Langmuir

Nematic Director Reorientation at Solid and Liquid Interfaces under Flow: SAXS Studies in a Microfluidic Device

Bruno F. B. Silva,*[,†,§] Miguel Zepeda-Rosales,[‡] Neeraja Venkateswaran,[†] Bretton J. Fletcher,[†] Lester G. Carter,[⊥] Tsutomu Matsui,[‖] Thomas M. Weiss,[‖] Jun Han,[⊥] Youli Li,[‡] Ulf Olsson,[§] and Cyrus R. Safinya*[,†]

[†]Department of Materials, Department of Physics and Department of Molecular, Cellular, and Developmental Biology and [‡]Materials Research Laboratory, University of California, Santa Barbara, California 93106, United States
[§]Division of Physical Chemistry, Lund University, P.O. Box 124, SE-221 00 Lund, Sweden
[‖]Stanford Synchrotron Radiation Lightsource, SLAC National Accelerator Laboratory, Menlo Park, California 94025, United States
[⊥]Paul Scherrer Institut, 5232 Villigen PSI, Switzerland

ⓢ Supporting Information

ABSTRACT: In this work we investigate the interplay between flow and boundary condition effects on the orientation field of a thermotropic nematic liquid crystal under flow and confinement in a microfluidic device. Two types of experiments were performed using synchrotron small-angle X-ray-scattering (SAXS). In the first, a nematic liquid crystal flows through a square-channel cross section at varying flow rates, while the nematic director orientation projected onto the velocity/velocity gradient plane is measured using a 2D detector. At moderate-to-high flow rates, the nematic director is predominantly aligned in the flow direction, but with a small tilt angle of $\sim\pm 11°$ in the velocity gradient direction. The director tilt angle is constant throughout most of the channel width but switches sign when crossing the center of the channel, in agreement with the Ericksen−Leslie−Parodi (ELP) theory. At low flow rates, boundary conditions begin to dominate, and a flow profile resembling the escaped radial director configuration is observed, where the director is seen to vary more smoothly from the edges (with homeotropic alignment) to the center of the channel. In the second experiment, hydrodynamic focusing is employed to confine the nematic phase into a sheet of liquid sandwiched between two layers of Triton X-100 aqueous solutions. The average nematic director orientation shifts to some extent from the flow direction toward the liquid boundaries, although it remains unclear if one tilt angle is dominant through most of the nematic sheet (with abrupt jumps near the boundaries) or if the tilt angle varies smoothly between two extreme values (~ 90 and $0°$). The technique presented here could be applied to perform high-throughput measurements for assessing the influence of different surfactants on the orientation of nematic phases and may lead to further improvements in areas such as boundary lubrication and clarifying the nature of defect structures in LC displays.
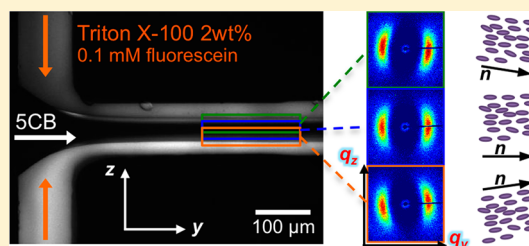
1. INTRODUCTION

Microfluidics involves the precise control and manipulation of fluids under submillimeter confinement.[1,2] The technology opens new exciting research and technological possibilities in dissipative systems out of equilibrium. A plethora of applications, such as lab-on-a-chip analysis, diagnostics, and particle synthesis, can be accessed, to mention a few examples. One particularly important highlight is the promise of new cheap technologies for health care, which are critical for underdeveloped countries.[3] Importantly, microfluidics can also be used as a probe for more fundamental studies. This is true not only to study phenomena where the micrometer-length scales are a relevant part of the phenomenon itself (e.g., blood rheology[4]) but also because many systems can be better controlled on micrometer-length scales where laminar flow regimes dominate, allowing the simultaneous control of experimental parameters that were previously hard to achieve

(e.g., rate of mixing, shear rate, concentration gradients, confinement, and geometry).[5,6]

The advantages of using such a platform for small-angle scattering are also enormous.[7−12] First, sample consumption is reduced to the microliter scale, allowing experiments with expensive and rare materials. Second, the constant flow of material prevents radiation damage (critical for X-ray synchrotron radiation). Third, flow-alignment effects can be used to our advantage, allowing a gain in resolution and the possibility to probe material properties and dynamic behavior that are usually not visible in nonoriented samples.[8,10]

Given the small length scales, confinement, and far-from-equilibrium conditions, unexpected phenomena can also arise. In some cases, very complex phenomena such as folding

instabilities can be simplified by the confinement of one of the dimensions/degrees of freedom to which the system could randomly evolve, allowing systematic studies to be performed.[13] Liquid crystals (LCs) have an intermediate degree of order between liquids and crystals,[14] and earlier work has shown that under flow, shear effects can induce unexpected out-of-equilibrium structural changes.[15−17] More recent studies of LCs under flow but now in microfluidic devices have also started to increase considerably.[5,18−27]

Nematic liquid crystals constitute the simplest example of liquid crystals. Here, the phase has only short-range positional order such as that in a regular liquid, but because of some specific molecular features (e.g., anisotropy, amphiphilicity), molecules exhibit a long-range orientational order, specified by a unit vector n, the nematic director.[14] This long-range orientational order gives rise to a wealth of interesting phenomena, the most famous being the application in liquid-crystal displays (LCDs). The orientation state of the nematic director n under flow is determined by the Ericksen−Leslie−Parodi (ELP) theory,[28−30] which considers the effects of the viscous Γ_v and elastic Γ_{el} torques on n. According to the ELP theory, the elastic torque vanishes at high shear rates (and hence flow rates), and only Γ_v is significant. When the ratio λ between the shear (γ_2) and rotational (γ_1) viscosities ($\lambda = -\gamma_2/\gamma_1$) meets the condition $|\lambda| > 1$ (the most common situation for nematics, including 5CB[31]), the stable solution of the equation of motion ($\Gamma_v = 0$) is then achieved when n aligns at a critical angle θ_S with the flow direction given by[14,28]

$$\theta_S = \frac{\cos^{-1}(1/\lambda)}{2} \qquad (1)$$

The presence of an interface may also lead to a preferred orientation. If the orientation imposed by the interface is different from that imposed by flow, then conflicting alignments may give rise to rich flow behavior. These effects can be greatly enhanced in microfluidic devices, where the small geometric length scales can accentuate the effects of conflicting surfaces, leading to, for example, director reorientations over smaller length scales than usual. This has been recently explored by Sengupta et al., who observed the emergence of different flow regimes resulting from the viscoelasticity of a nematic phase (5CB) accentuated at smaller channel gaps.[24] In a related approach, although without microconfinement, the combination between capillary flow alignment and SAXS was successfully employed to study the nematic−smectic transition.[32,33]

In this work, we are interested in the competition between flow and boundary conditions with respect to the orientation of nematic liquid crystals. By combining small-angle X-ray scattering (SAXS) with a microfluidic device, we describe an approach to measure the orientation of a flowing nematic liquid crystal directly under confinement near solid or liquid surfaces. For the solid-wall confinement, we use the microfluidic chip walls. For the liquid-wall confinement, we use the hydrodynamic focusing technique,[34] where a sheet of liquid is narrowed by a surrounding fluid. In the case of immiscible fluids, much of the attention has been placed on droplet formation under different regimes,[35] including nematic droplets.[18−20] Here, however, we aim to create stratified flows and inspect the nematic director orientation, with particular emphasis on the role of viscous forces from flow and surface anchoring forces imposed by the solid and liquid interfaces.

2. MATERIALS AND METHODS

5CB (4-cyano-4′-pentylbiphenyl) was purchased from Kingston Chemicals. Triton X-100 (poly(ethylene glycol) p-(1,1,3,3-tetramethylbutyl)-phenyl ether) was purchased from Sigma. Fluorescein was purchased from Aldrich. All of these chemicals were used as received. In all experiments, high-purity Millipore water was used. The microfluidic chips, made of cyclic olefin copolymer (COC or Topas) were purchased from Microfluidic ChipShop (catalog no. 02-0757-0166-02) and used without modification of the hydrophobic surface. The channel consists of four inlets meeting at a cross, with inlets 1−4 having lengths of 80, 5, 5, and 6 mm, respectively (Figure 1a). The
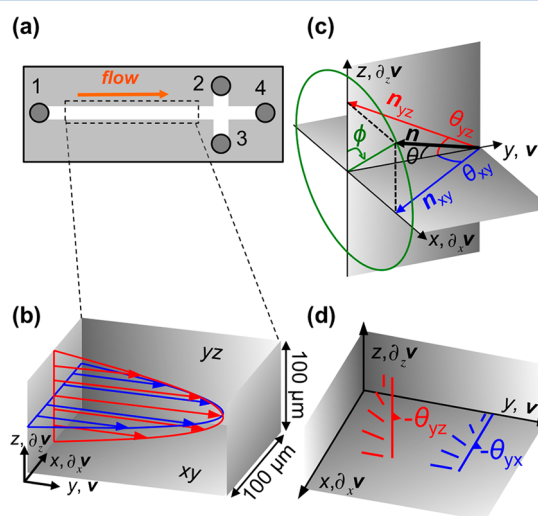

Figure 1. Illustration of the chip design, microchannel geometry, and coordinate system. (a) The flow is along the $+y$ direction (inlet 1 to outlets 2−4). (b) The channel cross section is square with a width of 100 μm. The velocity profile can be described with some level of approximation by a Poiseuille flow being maximized at the center of the channel and fading to zero at the surfaces as a result of the no-slip boundary condition. (c) Far from the edges, the nematic director n aligns preferentially along the velocity direction (y), making an angle θ in the velocity gradient direction (along x and z). ϕ is the angle between the velocity gradient and the z direction and defines the nematic director cone around the velocity direction y. θ_{yz} is the angle between y and n projected onto the $y−z$ plane (n_{yz}). θ_{yx} is the angle between y (velocity direction) and n projected onto the $y−x$ plane (n_{yx}). (d) Alternative visualization of θ_{yz}, the angle measured in the 2D SAXS detector ($y−z$ plane), and θ_{yx}.

microchannel cross section is square, with a width of 100 μm. In this work, contrary to what is more conventional, the main fluid flows in the reverse mode from what is usually the outlet along the main channel, meeting the cross at the end (Figure 1a). This method allows the study of pure 5CB in simple flow (without hydrodynamic focusing) along the main channel without perturbations from the cross. More importantly, in the hydrodynamic focusing experiments, allowing the nematic to flow in this direction helps to stabilize the nematic sheet and avoid the displacement of the LC into side channels 2 and 3.

In the simple flow experiments, a Nemesys syringe pump (Cetoni, Korbußen, Germany) was used. In the hydrodynamic focusing experiments, a custom-built step-motor-driven syringe pump system with three independently controlled pumps was used to drive fluid flow in the main channel and both side inlets. In both experiments, pulsation effects were not noticeable in the studied flow-rate range. Gastight syringes (500 μL, Hamilton) were used as pumps. Tygon tubing (formulation S-54-HL) with a 250 μm inner diameter was used. The tubing is connected to the syringes via a needle (gauge 29) with a suitable grip and connected to the microfluidic chip using custom-built connectors.[36]

For the hydrodynamic focusing experiments, the side fluid is a 2 wt % solution of Triton X-100, well above the cmc (0.019 wt %[37]). For the fluorescence microscopy observations, 0.1 mM fluorescein is added. The sample is mounted in a Nikon Diaphot 300 inverted microscope and imaged. For each flow rate, a stability test is performed to make sure the flow regime is stable. The stable flow rates are also approached from different paths to determine if they are robust or history-dependent (cf. section 3.2 for a discussion).

After the initial flow mapping through microscopy and the identification of stable flow regions, selected flow regimes are probed by SAXS. For the transmission SAXS measurements, the chip is mounted on a custom-built device holder, with translation capacity in the x, y, and z directions, and rotation of the β (about y) and γ (about x) angles (Figure 2a, bottom). Before the measurements, γ is aligned to zero with high precision. The β alignment is more complicated, and a maximum tilt angle of $\pm 2°$ can occur. The sample is placed normal to the X-ray beam and scanned in the z and y directions. The measurements were performed at two synchrotron facilities. The simple flow experiments were performed on the cSAXS beamline at the Swiss Light Source (SLS), Paul Scherrer Institute (PSI), Villigen, Switzerland. The hydrodynamic focusing experiments were performed on SAXS/D beamline 4-2 at the Stanford Synchrotron Light Source (SSRL), Menlo Park, CA, USA. For the cSAXS instrument, the X-ray wavelength (λ) used was 1.11 Å^{-1}, and the sample-to-detector distance was 2.16 m. The data was collected on a Pilatus 2 M detector. The beamline optics allowed a very small beam size of fwhm ≈ 6 μm in the z direction and 40 μm in the y direction. For the SAXS/D (BL 4-2) instrument, the X-ray wavelength (λ) used was 1.03 Å^{-1}, and the sample-to-detector distance was 1.1 m. Data was collected on a MX-225 Rayonix CCD detector. The X-ray beam had a size of ~30 μm (fwhm) in the z direction and 300 μm in the y direction. For both instruments, the obtained 2D scattering patterns were corrected for background by subtracting the 2D pattern of the chip outside of the microchannel corrected for the different thicknesses. The resulting 2D background-corrected patterns are subsequently analyzed with Matlab routines to extract structural information through q_h and q_l scans or the nematic director orientation through χ scans (Figure 2a, top).

3. RESULTS AND DISCUSSION

3.1. Nematic 5CB in Simple Flow under Solid-Wall Confinement.
Figures 1a,b show a simplified picture of the microchannel geometry, and Figures 1b−d show the coordinate system used in this work. The channel cross section (x−z plane) is square with a width of 100 μm (Figure 1b). Because of the micrometer-sized dimensions in both the z and x directions, the velocity gradient (or shear rate) extends in both of these directions (i.e., $\partial v_y / \partial x \neq 0$ and $\partial v_y / \partial z \neq 0$), and therefore there is no neutral direction. The velocity profile can be described with some level of approximation by a 2D Poiseuille flow, which is maximized at the center of the channel and fades to zero at the surfaces (no-slip boundary condition assumed, cf. Figure 1b). Importantly, throughout this work, the flow (velocity **v**) in the microchannel is always along the +y direction. The average orientation of a nematic liquid crystal is given by the director n, and far from the walls, n tends to align along the velocity direction (y axis) but with an angle θ with **v** (Figure 1c,d). Because of the square geometry, the velocity gradient extends over both the x and z directions (cf. Figure S3); therefore, the director can rotate about a cone determined by a second angle ϕ (i.e., rotation about the y axis) in which not changing the magnitude of θ changes its projection in the y−z plane (containing **v** and ∂_z**v**) and y−x plane (containing **v** and ∂_x**v**) (Figure 1c). $\phi = 0°$ in the vicinity of the horizontal walls ($z = z_{wall} = \pm 50$ μm), and $\phi = 90°$ in the vicinity of the vertical walls ($x = x_{wall} = \pm 50$ μm). Anywhere in the channel (away from the walls), $\phi(x, z)$ can be calculated from the velocity
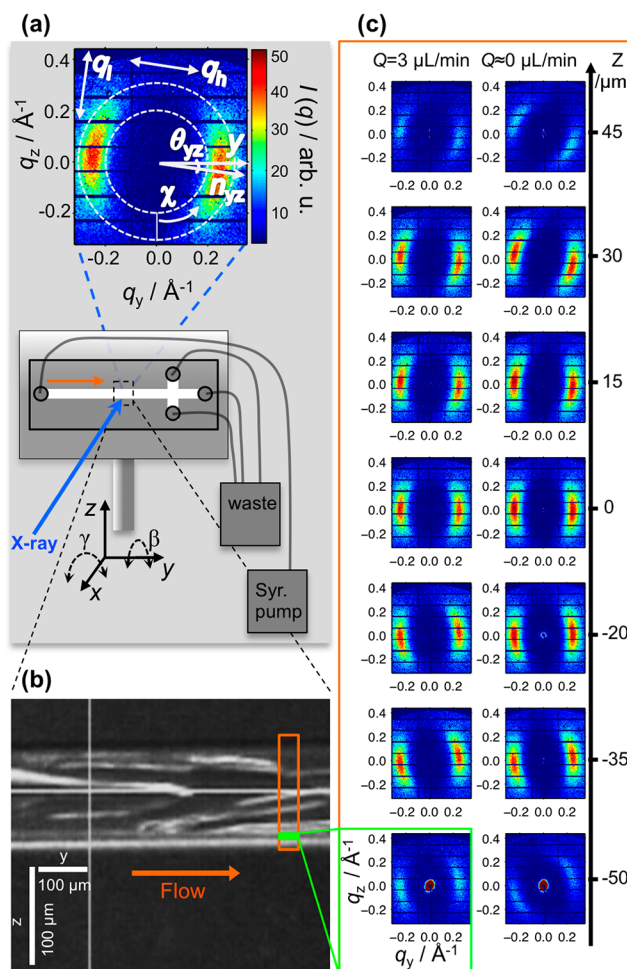

Figure 2. Summary of the microfluidic SAXS experiments. (a) Typical SAXS pattern (top) and schematic of the microfluidic device (bottom). The device holder (shown at the bottom) can be translated in the x, y, and z directions and rotated in β (about y) and γ (about x). The X-ray beam is along the x direction, and the SAXS pattern (in the q_y, q_z plane) is collected in a detector behind the device. In both the chip and detector, the flow is along the +y direction. A typical SAXS pattern (flow rate Q = 3 μL/min, z = 30 μm) at small q is dominated by the nematic phase correlation peak, which is inversely proportional to the nearest-neighbor distance between the nematogens along their main axis. Therefore, the peak maximum $q = 2\pi n/d$ is along the nematic director n projected onto the y−z plane (n_{yz}), and θ_{yz} is the angle between n_{yz} and the flow direction (y). The direction q_h is defined as being parallel to n_{yz}, and q_l is perpendicular to n_{yz}. In our convention, $\chi = 0°$ is the negative q_z axis, and the positive rotation is counterclockwise. (b) Snapshot of 5CB flowing slowly (approaching 0 μL/min) before data acquisition at the cSAXS beamline. Nematic Schlieren-like flowing textures can be seen even without polarized light. The green box represents the X-ray beam's fwhm (~6 μm along z and ~40 μm along y) and hence the area probed by each X-ray measurement. The orange box represents a typical area probed in a vertical scan (z intervals of 4.85 μm). (c) Representative scattering patterns of a flowing nematic phase recorded along the width (z direction) of the microchannel at a flow rate of 3 μL/min (left) and at rest (right). The patterns rotate with roughly mirror symmetry with respect to the center of the channel (clockwise in the upper part of the channel (+z) and counterclockwise in the lower half (−z)). Close to the edges, the magnitude of the rotation is larger at rest. At the edges of the microchannel, the scattering intensity is also lower because approximately half of the X-ray beam is outside of the microchannel and may have a contribution from the y−x plane due to a small tilt (<2°) of the device in β.
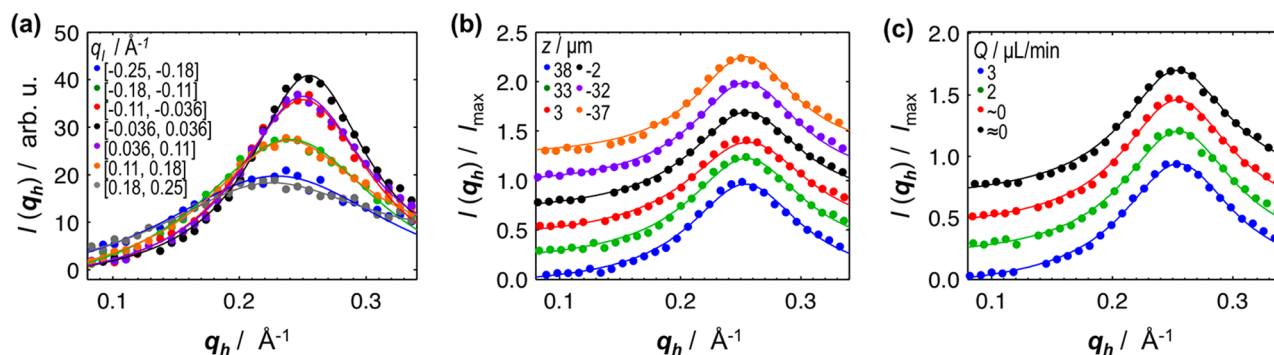
Figure 3. One-dimensional scattering profiles of the 5CB nematic confined in the microfluidic device. The coordinates (q_h and q_l) in reciprocal space are defined in Figure 2a (top). (a) q_h scans integrated over different q_l intervals in the center of the channel ($z \approx 0 \ \mu m$) at a flow rate of $Q = 3 \ \mu L/$min. (b) q_h scans (integrated over a q_l range from -0.036 to $0.036 \ Å^{-1}$) at $Q = 3 \ \mu L/min$ and at different z positions along the channel (cf. Figure 2c, which shows that the z range goes from ~ -50 to $\sim +50 \ \mu m$). The proximity to the microchannel boundaries does not modify or distort the 1D profiles integrated over q_l. (c) q_h scans (integrated over the q_l range from -0.036 to $0.036 \ Å^{-1}$) at different flow rates. The 1D profiles are not modified or distorted in the investigated flow rates. In both (b) and (c), the curves are normalized and slightly offset for ease of visualization. In all panels (a−c), the circles constitute scattering data and the lines constitute Lorentzian fits.

gradient profile in the x−z plane, according to $\phi = \tan^{-1}(\partial_x \mathbf{v}/\partial_z \mathbf{v})$. Importantly, $\theta_{yz} = \tan^{-1}(\cos \phi \tan \theta)$ is the projection of θ in the y−z plane (the 2D-detector plane in the SAXS regime) and is equal to θ when $\phi = 0$. θ_{yz} is the orientation angle measured in our microfluidic SAXS setup (Figures 1c and 2a). $\theta_{yx} = \tan^{-1}(\sin \phi \tan \theta)$ is the projection of θ in the y−x plane and is equal to θ when $\phi = 90°$.

The flow rate Q is varied from 3 to $\approx 0 \ \mu L/min$, covering a range of shear rates $\dot{\gamma} = 200$ to $\approx 0 \ s^{-1}$ (Table S1). After we switch to a new flow condition, 10−30 min of waiting is allowed before the next measurement starts. Below $0.1 \ \mu L/min$, the pump is switched off, and after 10 min, a new scan is started, which we denote as Q approaching $0 \ \mu L/min$. Throughout the duration of the scan (10 min), the phase continued flowing slowly, as observed with the video camera. After this measurement, we waited 30 min more before a new scan was started, which we denote as $Q \approx 0 \ \mu L/min$. In this last scan, no noticeable movement could be detected in the channel.

Figure 2 shows the experimental setup used for SAXS data collection and an example of a 2D SAXS pattern in reciprocal (q_h, q_l) space (a), a snapshot of 5CB in the microfluidic chamber at a low flow rate (b), and a series of 2D SAXS patterns with the X-ray beam going through different positions (z) across the width of the microfluidic channel (c). Each SAXS pattern corresponds to a displacement in the z direction (across the width of the channel) with a step size of $4.85 \ \mu m$. The incident X-ray beam is along the x direction. The SAXS pattern collected by a 2D detector is displayed with the same orientation as for the microfluidic device.

The SAXS pattern is dominated by a broad peak centered at $q_h = 0.254 \ Å^{-1}$ (Figure 2a,c). This peak results from the short-range positional liquid order between nearest neighbors along the direction parallel to n. Hence, the azimuthal (in plane) orientation of the peak directly gives the orientation of n projected onto the y−z plane (i.e., n_{yz}). In other words, the SAXS patterns directly give the director angle projection onto the y−z plane: θ_{yz}. The peak is not perfectly radially symmetric but is somewhat extended in the q_l direction. As such, normal azimuthal integration smears the pattern to some extent. For this reason, we choose to integrate the intensity in projections along the q_l and q_h directions (Figure 2a, top). The most striking effect that can be seen in Figure 2c is the variation in

the peak orientation as we scan along z. The rotation in the 2D SAXS patterns exhibits roughly mirror symmetry with respect to the center of the channel ($z = 0 \ \mu m$) i.e. θ_{yz} (the angle between the axis connecting both peaks and the y axis, Figure 2), is approximately zero in the middle of the channel, and rotates clockwise in the upper half of the channel (+z) and counterclockwise in the lower half ($-z$). This effect also seems to be pronounced at rest ($Q \approx 0 \ \mu L/min$) because the tilt in θ_{yz} seems to be larger when compared to $Q = 3 \ \mu L/min$.

Figure 3a shows q_h scans through the peak maximum ($q_h = 0.254 \ Å^{-1}$) of 5CB at $Q = 3 \ \mu L/min$ for the 2D SAXS patterns at $z = 0 \ \mu m$ (Figure 2c) averaged over different q_l intervals. Real-space dimension $d = 2\pi/q = 24.7 \ Å$ is ca. 1.4 times the size of a 5CB molecule, in good agreement with the suggestion that 5CB molecules are predominantly in a dimeric form, with their benzene rings forming a pair, and the alkyl chains protruding outward.[38,39] The half-width at half-maximum (hwhm) of the peak is $0.057 \ Å^{-1}$. This corresponds to a correlation domain with $\sim 1/0.057 \ Å^{-1} = 17.5 \ Å$, which is expected for liquids with near-neighbor short-range positional order.

In Figure 3b, q_h scans of the central region of the pattern (q_l interval of -0.036 to $0.036 \ Å^{-1}$) are shown for z at the center and close to the edges of the channels. As shown, no noticeable differences can be spotted between the curves, and the peak positions remain the same. This extends also to the case of no shear, in which the peak position and width are essentially the same (Figure 3c). This indicates that flow effects are not distorting the short-range positional order of the nematic liquid crystal. Instead, these effects result in changes in the orientation of n, which is the most common situation for nematics under flow.[15]

The most important flow effect in the current system—the shift in the director orientation—is more clearly seen in azimuthal χ scans in the (q_h, q_l) plane (Figure 2a, top). By fitting the peak positions in χ, one could quantitatively obtain the projection of director orientation θ_{yz} (cf. Figure 1). We fit the peaks with a double Lorentzian equation of the form

$$I(\chi) = \frac{A_1}{b_1^2 + (\chi - \chi_0)^2} + \frac{A_2}{b_2^2 + (\chi - 180 - \chi_0)^2} + c \tag{2}$$

where we restrict the position χ_0 of peak 2 to exactly 180° away from peak 1 because both peaks are related through a two-fold

rotational axis. A_1 and A_2 are proportional to the heights of peaks 1 and 2, b_1 and b_2 are the hwhm's of the peaks, and $c \approx 0$ is a constant related to the background.

In Figure 4, normalized χ scans and respective fits are shown for $Q \approx 0\ \mu L/min$. As can be seen, when going from the top to
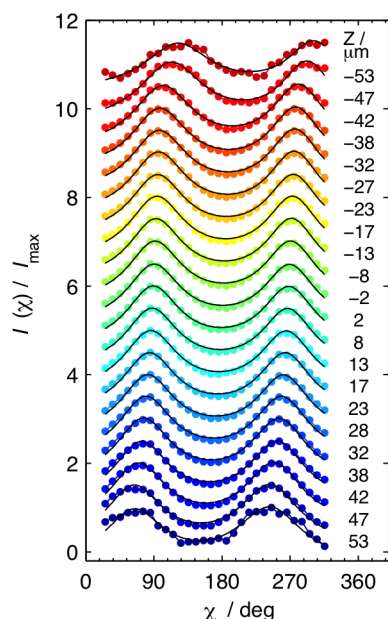

Figure 4. χ scans and respective double-Lorentzian fittings (cf. Figure 2a, top, for the definition of angle χ in the (q_h, q_l) plane) measuring the orientational width of the nematic correlation peak for 5CB in a microfluidic device at $Q \approx 0\ \mu L/min$. Data is normalized and displaced along the ordinate axis for ease of visualization. The quality of the data (and hence the fitting) is reduced at the edges of the microfluidic device ($z \approx \pm 53\ \mu m$), as a result of part of the X-ray beam being outside the microchannel and hence not hitting the 5CB nematic.

the bottom of the channel (bottom to top in Figure 4a), χ_0 shifts from ca. 61° at $z = 53\ \mu m$ to ca. 124° at $z = -53\ \mu m$. In between, $\chi_0 \approx 90°$ at $z = 0\ \mu m$. Because the flow direction is along the y axis and is at an angle of $\chi = 90°$, the director angle with the flow direction θ_{yz} is directly extracted through $\theta_{yz} = \chi_0 - 90°$.

In Figure 5a,b, we show the dependence of θ_{yz} on z for flow rates of $0.2\ \mu L/min \leq Q \leq 3\ \mu L/min$ and $Q < 0.1\ \mu L/min$. Note that to facilitate the observation of symmetry (or lack thereof) of θ_{yz} across z with a mirror plane in the middle of the channel ($z = 0\ \mu m$), we display the absolute value $|\theta_{yz}|$ instead. Also, for easier association of the θ_{yz} dependence with the Poiseuille profile, the abscissa θ_{yz} is displayed in reverse order. Immediately evident is the fact that for $Q \geq 0.2\ \mu L/min$ all of the curves overlap very well. Likewise, Q approaching 0 and $Q \approx 0\ \mu L/min$ also display very similar profiles to each other. More striking is the obvious difference in curve profiles between the $Q \geq 0.2$ and $Q < 0.1\ \mu L/min$ groups. In all cases, θ_{yz} is negative (clockwise rotation) in the upper half of the microchannel ($z > 0$) and is positive (counterclockwise rotation) in the lower half ($z < 0$). The same information can be seen in Figure 5c for flow rates of $Q = 3\ \mu L/min$ and $Q \approx 0\ \mu L/min$ and where the nematic director projection n_{yz} orientation is represented in the form of an orientation field as a function of z and y. Figure 5d shows a schematic of the 5CB molecules and nematic director orientation and corresponding 2D SAXS patterns.

Under pressure-driven flow (e.g., Poiseuille flow), far from the boundaries, and when the ratio λ between the rotational (γ_1) and shear (γ_2) viscosities ($\lambda = -\gamma_2/\gamma_1$) meets the condition $|\lambda| > 1$ (which is the case for 5CB[31] and most known nematics), the torque Γ on the nematic director usually vanishes when the director aligns at a critical angle (eq 1) $\theta_S = \cos^{-1}(^1/_\lambda)/2$ (henceforth called the shear angle) between the flow and gradient directions.[28] If the orientation imposed by the surface is different from the alignment imposed by flow, then a transition layer of length $e_1 \approx (K/\eta\dot{\gamma})^{1/2}$ (where K is related to the nematic-phase elastic constant[14] and η is an average nematic LC viscosity, cf. SI) close to the surface will occur, where the director gradually shifts from the boundary orientation to the flow orientation. In addition, because the velocity field is symmetric about the center of the channel, θ switches signs in the center along a transition region of size[14] $e_2 \approx (h e_1^2)^{1/3}$ ($h = 100\ \mu m$ gap size in a microfluidic device). It is therefore important to determine if the observed variation in θ_{yz} with z is an effect of confinement, where the boundary layers could have a greater influence on the orientation field far from the walls or they are simply a consequence of the fact that SAXS data measures θ_{yz} (the projection of θ on the $y-z$ plane) rather than θ directly (cf. Figure 1d).

As shown in Figure 1c,d, θ is the angle between the nematic director n and the velocity (or flow) direction y. ϕ is the angle measuring the rotation of n about the y axis. The projection of θ in the $y-z$ plane (SAXS detector plane) is given by $\theta_{yz} = \tan^{-1}(\cos\phi\tan\theta)$. To compare our results with Leslie's solution, we assume a θ profile equal to θ_S throughout the whole microchannel except within the boundary layer e_2, where for simplicity θ decreases linearly from $\theta = \theta_S$ at z and $x = \pm e_2$ to $\theta = 0°$ at z and $x = 0$ (Figure S2 in SI). (e_1 is neglected because our measurements in the vicinity of the channel walls are not accurate.) To obtain ϕ, we require the 2D velocity profile ($\mathbf{v}(x, z)$) from which the velocity gradients can be calculated (Figures S1 and S2 in SI). From the velocity gradient components in the x and z directions, ϕ is easily obtained ($\phi = \tan^{-1}(\partial_x\mathbf{v}/\partial_z\mathbf{v})$). θ_{yz} is then computed as a function of x and z using the respective $\theta(x, z)$ and $\phi(x, z)$ and subsequently averaged over the x direction to obtain $\theta_{yz}(z)$. A further step in the fitting includes finite beam size effects. In the fitting, we compare two different velocity profiles. We use the normal Poiseuille flow, which yields a parabolically shaped velocity profile and is suitable for Newtonian fluids under laminar flow. Because the nematics are non-Newtonian, the actual flow profile deviates slightly from the parabolic shape, and we also use the flow profile determined by Jewell et al. for 5CB flowing in a microchannel with a rectangular geometry.[40] A more detailed description of the fitting procedure can be found in the Supporting Information. As can be seen in Figure 5a, both models (Poiseuille, red curve; non-Newtonian, blue curve) fit the data reasonably well for $\theta_S = 11°$, which validates the use of the Poiseuille flow profile as an approximation in this case. More importantly, the goodness of the fits confirms that the Leslie solution holds under these conditions ($Q > 0.1\ \mu L/min$). The variations in the observed shear angle as a function of z therefore most likely results from the azimuthal angle ϕ, which varies from 0 to 90° (as a result of the equivalence of walls $y-x$ and $y-z$ in the square cross section) and decreases the projection of angle θ in the SAXS detector plane ($y-z$). Using $\theta_S = \cos^{-1}(^1/_\lambda)/2$ (eq 1), one can extract λ from the determined θ_S, obtaining $|\lambda| = 1.08$, which is in reasonable agreement with the values of $|\lambda| = 1.12$ and $\theta_S = 13°$ reported
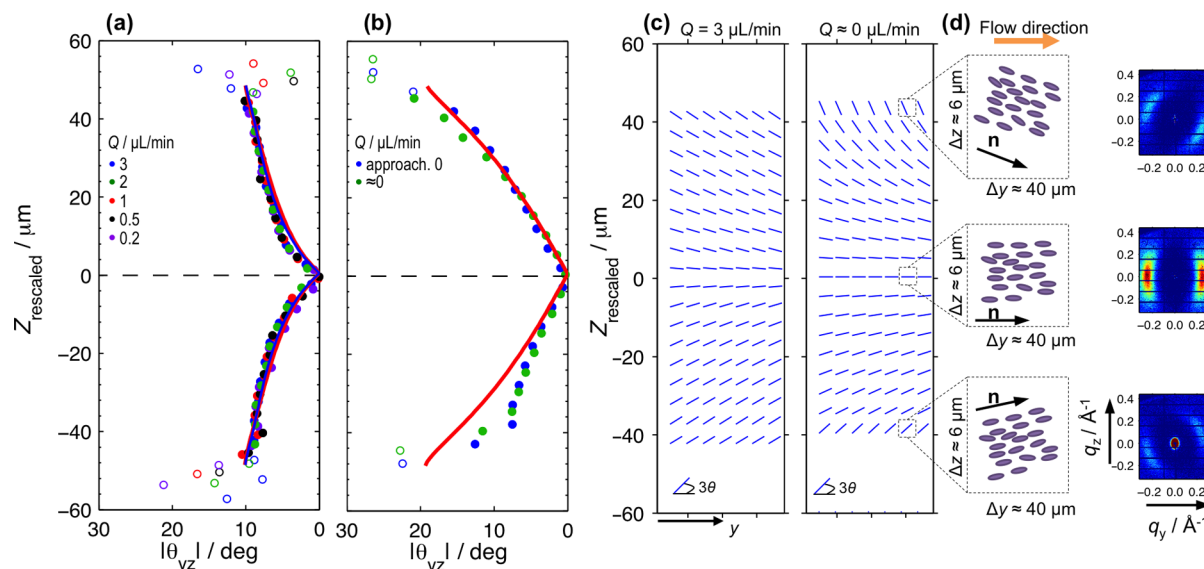
Figure 5. Fitting results for the nematic director angle projection θ_{yz} at different z positions along the microchannel (cf. Figure 1c for the definition of θ_{yz}). Results for the (a) 0.2 μL/min $\leq Q \leq$ 3 μL/min and (b) $Q < 0.1$ μL/min regimes. The z position is rescaled by centering $\theta = 0°$ at $z_{rescaled} = 0$ μm. Note that the abscissa represents $|\theta_{yz}|$ in reverse order for ease of visualization because the resulting $z - \theta_{yz}$ dependence resembles the Poiseuille flow profile. Solid data points result from X-ray patterns where the beam is mostly inside the microchannel in the $y-z$ plane. Open data points result from patterns where a significant fraction of the X-ray beam was hitting outside of the $y-z$ plane, catching part of the $y-x$ plane because of a small rotation of the microfluidic device holder about the y axis parallel to the flow (i.e., the β angle shown in Figure 1a). Note that some points close to $z = 55$ μm shift to smaller angles. A clear distinction in the flow profiles can be seen for $Q \geq 0.2$ and $Q < 0.1$ μL/min. In the first group (a), the director tilt is controlled by flow (i.e., the Leslie solution discussed in the text, where the nematic director assumes a dominant angle $\pm\theta_S$). The red and blue lines represent the Leslie solution for $\theta_S = 11°$ using the Poiseuille and non-Newtonian velocity profiles, respectively (which are very similar). In the second group (b), boundary effects are more predominant. The line represents the escaped director configuration model (eq 3) assuming $R = 71$ μm (half of the diagonal length of the square channel), resulting in θ_R (the angle of n at the surface) = 32°. (c) Schematic representation of the orientation of the nematic director as a function of microchannel z position for $Q = 3$ and ≈ 0 μL/min. Each blue bar represents the average orientation of a rectangle with height $\Delta z \approx 6$ μm and length $\Delta y \approx 40$ μm (the fwhm of the beam profile). The director angle θ_{yz} is multiplied by 3 to facilitate visualization of the changes across z and for the different Q values. (d) Schematic illustration of the molecular arrangement for selected points along the orientation field in (b) and respective X-ray scattering patterns.

elsewhere.[31] One should also note that even though e_2 (and e_1) depends on $\dot{\gamma}$, our data does not change in the range of 0.2 μL/min $\leq Q \leq$ 3 μL/min (Figure 5a). This is mainly a result of θ being convolved with ϕ.

As we see in Figure 5b, at a low flow rate below 0.1 μL/min the behavior is very different. The variation of θ_{yz} with z now has an almost linear dependence. (There is a small lack of symmetry that is discussed in the SI.) Despite the movement of 5CB in the microchannel, clearly seen in the camera and microscope at Q approaching 0 μL/min, θ_{yz} has reoriented across the whole channel, except at $z = 0$ μm where θ_{yz} is still zero. Even though in our measurements we can only probe the projections on the $y-z$ plane, it is very likely that this relaxation also takes place across x. Hence, the line parallel to y in the center of the channel at x and $z = 0$ μm is almost a smoothed disclination line, where θ_{yz} (and θ_{yx}) takes opposite signs on each side of this line. This configuration resembles the escaped radial configuration (typically observed in tubes of cylindrical[41,42] and square[24] cross sections at rest, where the nematic director reorients near the central region of the channel along the channel axis in order to accommodate competing orientation demands from walls perpendicular to each other).

In the cylindrical geometry, at rest or low flow, where boundary conditions and elastic energy terms dominate, the angle between the director and cylinder axis (approximately equal to our condition with a square cross section) (θ) can be described by[42]

$$\theta(r) = 2 \tan^{-1}\left(\frac{r}{R}\tan(\theta_R/2)\right) \tag{3}$$

where r is the radial distance from the center of the cylinder, R is the cylinder radius, and θ_R is the angle of n at the surface (for strong homeotropic anchoring, $\theta_R = 90°$). This equation, convoluted with the $\phi(x, z)$ profile and beam size, fits our data to some degree (Figure 5b), resulting in $\theta_R = 32°$ if R is taken to be 71 μm (half of the diagonal of our square geometry). If θ_R is fixed to $\theta_R = 90°$ (strong homeotropic anchoring) and we fit R instead, then we obtain $R = 250$ μm. This could indicate either weak surface anchoring or nonhomeotropic alignment. However, one also has to recall that the above equation was derived for cylindrical geometry. In the case of square geometry, the elastic deformation that causes the escaped configuration is already very significant at the corners of the channel, which may force the escaped configuration to change more abruptly than what eq 3 would predict for cylinders. Hence, it is not clear on the basis of these measurements if the anchoring is strong or weak. It is our view that the observed behavior is in better agreement with a situation of strong anchoring. Note that we started at $Q = 3$ μL/min and slowly decreased the flow rate until $Q \approx 0$ μL/min, which resulted in the strong preorientation of the director in the flow field. Given the fact that stopping the flow leads to a relaxation of the preoriented profile, with the director reorienting all of the remaining θ, except the "disclination" line at x and $z = 0$, then this should give a hint that the elasticity emanating from the

boundary condition is strong. In any case, regardless of strong or weak anchoring, it is evident that at low flow rates ($Q < 0.1$ μL/min) the elasticity (resulting from competing preferential homeotropic alignment at the walls) becomes dominant.

To conclude this section, we stress that through our microfluidic SAXS measurements we were able to directly probe the nematic director orientation profile of a nematic liquid crystal flowing in a microchannel with micrometer resolution in z and identify two different flow regimes (one for 0.2 μL/min $\leq Q \leq 3$ μL/min and the other for $Q < 0.1$ μL/min). Our results confirm what was anticipated by Sengupta et al.[24] for the strong flow regime (high flow rates). By using channels with rectangular cross section, the interesting intermediate and weak flow regimes observed in that work are also expected to be suitably determined. One advantage of our method compared to microscopy is the ability to obtain a more quantitative description of the director tilt across the channel. The tilt angle can be accurately determined, with its resolution being only limited by the averaging effects from the beam size and by the shift in the angle projection due to the azimuthal orientation. (Note that the azimuthal shift is caused by the square cross-section. Hence, resolution can be significantly improved by using channels with a rectangular cross section of high aspect ratio.) Another advantage of this present method is the ability to map changes in the molecular arrangements of the fluid simultaneously. Here we clearly demonstrated that despite reorientation the nematic peak position and width remain the same, indicating that the studied flow conditions do not affect the local arrangements of the fluid simultaneously with the director orientation. This may not always be the case in lyotropic systems that are more compressible and where concentration fluctuations and instabilities induced by flow can occur.[43]

3.2. Liquid-Wall Confinement: Hydrodynamic Focusing.

In section 3.1, we described the alignment of 5CB and the interplay between viscous and surface forces in simple flow, where the boundary conditions are due to the walls of the microchannel (solid interfaces). In this section, we describe a similar approach, but where the nematic liquid crystal is bound by flowing liquid from above and below (liquid interfaces) and where capillary forces arising from the interfacial tension between the immiscible fluids (nematic and water with some dissolved surfactant) also play an important role. For this purpose, we employ the technique of hydrodynamic focusing.[20,34,44] In this experiment, 5CB flows along the main channel (channel 1, cf. Figure 6a,b) as before, with a flow rate of Q_m, but now a solution of 2 wt % Triton X-100 also flows in channels 2 and 3 at a flow rate of Q_s (Figure 6a). The ratio of the total flow rate from the side channels ($2Q_s$) to the flow rate of the middle fluid (Q_m) is $r_Q = 2Q_s/Q_m$. The three fluids meet at the cross and flow together into the outlet (channel 4). For a suitable range of flow rates Q_m and flow rate ratios r_Q between 5CB and the triton solutions, stable sheets of 5CB with fluid on both sides can form (Table S2 and Figure 6c,d). The nematic sheet was found to be stable for a surfactant solution total flow rate of $2Q_s = 24$ μL/min, with 5CB flowing in the range of $Q_m = 1$ to 3 μL/min (Table S2). At lower $Q_m < 1$ μL/min, jetting occurs, with a thin thread of 5CB forming for a limited length ($\sim$200−300 μm) before rupturing to form droplets. At higher $Q_m > 3$ μL/min, displacement instabilities[44] occur, leading to an invasion of middle fluid 5CB into the side channels. The system is also stable when increasing Q_m while keeping the same flow rate ratio r_Q, but the same does not happen when Q_m
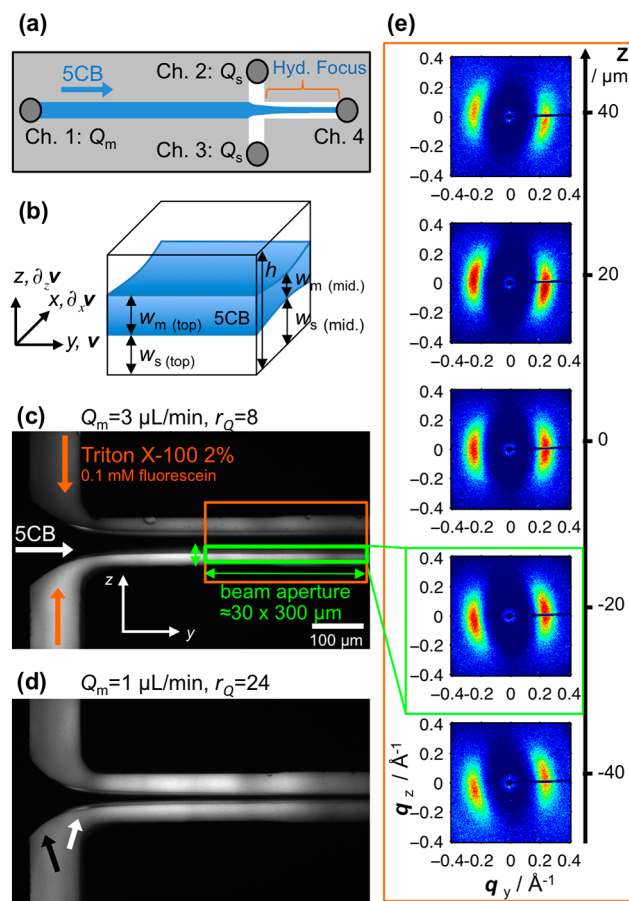

Figure 6. Summary of the hydrodynamic focusing experiments with the nematic phase of 5CB confined in a microfluidic device by solid and liquid interfaces. (a) Schematic representation of the experiment. 5CB flows along channel 1 and is focused into channel 4 by the side fluids (2 wt % Triton X-100 in water) coming from channels 2 and 3. This setup facilitates the formation of stable nematic sheets. (b) Schematic representation of the 5CB nematic sheet focused by the Triton solution. (c) Micrograph of a typical hydrodynamic focusing experiment. Here the side fluids contain 0.1 mM fluorescein to facilitate the visualization of the nematic sheet (black). 5CB flows at 3 μL/min, and each side fluid flows at 12 μL/min ($r_Q = 2Q_s/Q_m = 8$). The width of the nematic sheet is ca. 46 μm on the top and ca. 19 μm in the middle of the channel. The green box represents the X-ray beam's fwhm ($\sim$30 μm along z and $\sim$3000 μm along y) and hence the area probed by each X-ray measurement. The orange box represents a typical area probed in a vertical scan (z intervals of 10−20 μm). (d) The same as in (c) but with a 5CB flow rate of 1 μL/min and $r_Q = 24$. The focused nematic sheet seems to have a concave shape along the x direction (note the relief pattern indicated by the white arrow compared to the dark arrow for the formation of the sheet), with its width being ca. 22 μm on the top and ca. 8 μm in the middle of the channel. (e) SAXS along the width of the channel for $Q_m = 3$ μL/min, $r_Q = 8$. As in the simple flow experiments, here also the nematic director rotates from a negative θ_{yz} on the top to a positive θ_{yz} on the bottom side of the sheet.

is lowered at constant r_Q. This is because the system becomes more sensitive to small perturbations. The middle fluid 5CB is not surrounded by side fluid in all directions. Instead, it is surrounded by side fluid along the z direction, in which the y−x interfaces are now the side fluid, but along the x direction, it is still bound by the chip walls (y−z surfaces, Figure 6b). (Note in Figure 6d that in the nematic region there is no trace of fluorescence. Furthermore, the relief pattern indicated by the
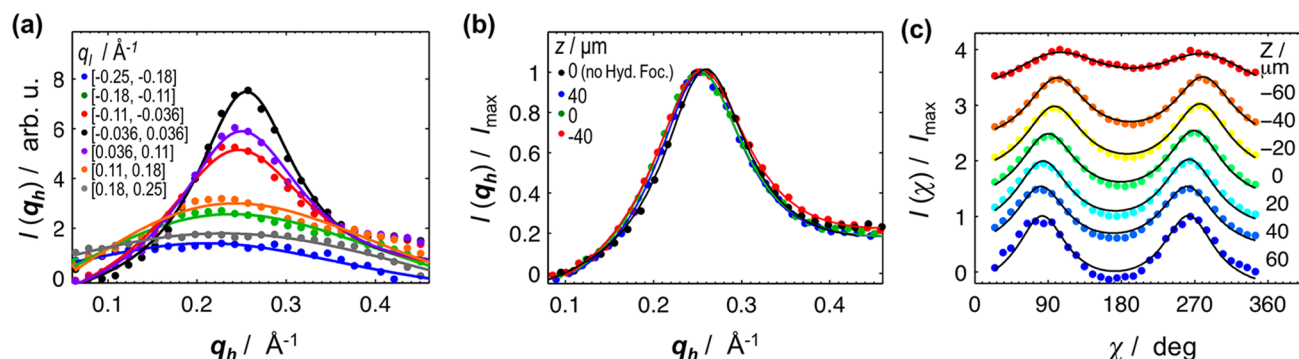
Figure 7. One-dimensional scattering profiles of hydrodynamically focused flowing 5CB. The coordinates (q_h, q_l) and angle χ in reciprocal space are defined in Figure 2a. (a) q_h scans integrated over different q_l intervals in the center of the channel ($z \approx 0$ μm) for a hydrodynamic focusing experiment. The flow rate of 5CB (middle channel) is $Q_m = 3$ μL/min, and the ratio $r_Q = 2Q_s/Q_m$ of the combined side fluids (Triton X-100 2% solutions) with the inner fluid is $r_Q = 8$. (b) Comparison between q_h scans (integrated over $q_l = -0.036$ to 0.036 Å^{-1}) in the system with no hydrodynamic focusing (black, $Q = 3$ μL/min) and the hydrodynamic focusing system ($Q_{5CB} = 3$ μL/min, $r_Q = 8$). All hydrodynamic focusing patterns show a slight shift in the peak position to lower angles ($\Delta q \approx 0.006$ Å^{-1}), which may indicate a slight penetration/contamination of Triton or Triton/water particles within the 5CB sheet. Nonetheless, given the very small shift in the peak, both the contamination and resulting structural changes should be minimal. (c) χ scans and respective double-Lorentzian fittings for a hydrodynamic focusing run with $Q_m = 3$ μL/min and $r_Q = 8$. Data is normalized and displaced along the ordinate axis for ease of visualization. In all panels (a–c), circles constitute scattering data and lines are Lorentzian fits.

white arrow suggests a concave shape of the nematic sheet.) It was found that $Q_m = 3$ μL/min with $r_Q = 8$ is the most stable flow condition. For lower Q_m (< 1.5 μL/min), the flow condition becomes history-dependent because the nematic stream is not able to form by itself but remains stable if it is formed at higher Q_m and then decreased slowly to the final value.

Hamlington et al. have studied the coflow of 5CB and silicon oil. Although the goal was the formation of nematic droplets, stable stratified flow regimes were also identified. In addition to capillary and viscous forces, wetting of the device walls by 5CB was identified as an important parameter stabilizing the nematic sheet. The non-Newtonian nature of 5CB and defect structures, however, cause instabilities that promote droplet formation.[20] In a more general study, although restricted to Newtonian fluids, Cubaud and Mason have studied different flow regimes between coflowing immiscible liquids with different viscosities and interfacial tension contrasts, with the flow regimes being mapped into a flow map of capillary number Ca in middle fluid Ca_m versus side fluid Ca_s.[44] The interfacial tension between 5CB and water has been reported to be approximately 26 mN/m.[45] This leads to a predominance of capillary over viscous forces, which does not allow the formation of a stable nematic sheet of liquid. Instead, the system drips, with the immediate formation of droplets (i.e., to reduce the surface energy cost), in agreement with the flow map.[44] The addition of 2 wt % Triton X-100 reduces the interfacial tension, allowing the formation of nematic sheets sandwiched between two aqueous surfactant solutions (Figure 6c,d). Also important for the stabilization of the sheets against breakup is the poor wettability of the microchannel walls by the side fluid when compared to that by the nematic fluid.[20] (Note that the hydrophobic channel walls should have more affinity for 5CB than for water.)

The nuances of the flow map and the role of capillary and viscous forces coupled with the non-Newtonian behavior will be the subject of a more detailed study elsewhere. In this work, we are mainly interested in the effect of the liquid boundaries on the nematic director. Note that despite the nematic sheet being bound by liquid interfaces at $\pm w_m/2$ μm and solid surfaces at ± 50 μm, 5CB is squeezed along the z direction,

reducing the contact with the solid walls. Hence, the liquid boundaries ($y-x$) become dominant. Also, as noted previously, in these SAXS measurements, what is measured is θ_{yz}, which is the projection influenced by the liquid boundaries.

At the synchrotron, two flow conditions were studied: $Q_m = 3$ μL/min, $r_Q = 8$; and $Q_m = 1$ μL/min, $r_Q = 24$. In Figure 6e, 2D SAXS profiles due to scattering from the hydrodynamically focused 5CB at different positions along the z axis are shown. As in the simple flow experiment, the same rotation in the nematic director is observed, with θ_{yz} being negative in the upper half of 5CB and positive in the lower half. In this case, the beam size is much larger (fwhm ~30 μm), which introduces much stronger averaging effects but is still suitable for an overall determination of the focused nematic stream. The larger scanning step size (10 and 20 μm) also needs to be taken into account. Figure 7a shows q_h scans averaged over different q_l intervals at $Q_m = 3$ μL/min, $r_Q = 8$, and $z = 0$ μm. In Figure 7b, q_h scans of the central region of the pattern (q_l interval of -0.036 to 0.036 Å^{-1}) are shown across the nematic stream, in contact with the Triton solutions, and compared to the pure system. All hydrodynamic focusing patterns show a slight shift in the peak position to lower angles ($\Delta q \approx 0.006$ Å^{-1}), which may indicate a slight penetration/contamination of triton or triton/water particles within the 5CB sheet. Even though this shift in the peak is very small, this phenomenon is occurring mainly on the interface, which makes the signal weaker compared to that of the remaining nematic sheet. Hence, greater structural changes cannot be discarded. We also note that although the residence time of 5CB in the channel is small (~0.1 s), the surfactant concentration is two orders of magnitude above the cmc (0.019 wt %[37]), which could lead to some solubilization of 5CB at the interface and lead to some instabilities that could affect the observed results.

As with the simple flow case (cf. section 3.1), also here it is convenient to extract θ_{yz} from the χ scans. Figure 7c shows the resulting fits of scans with the double-Lorentzian expression (eq 2). Figure 8 shows a plot of the measured θ_{yz} at different z positions along the channel. The data extends over a wider z range than the widths of the nematic sheets w_m. This results from the fact that the beam size (fwhm ≈ 30 μm) is larger than
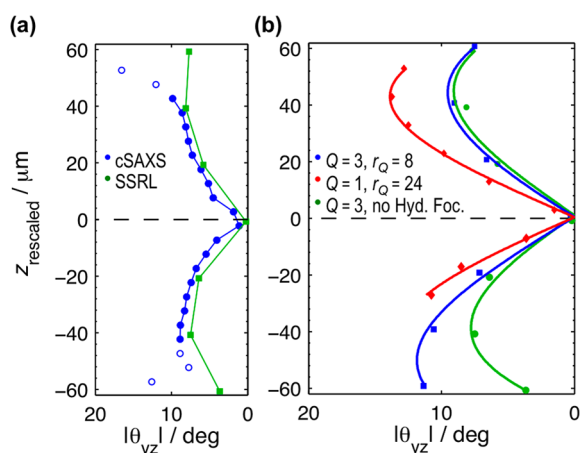
Figure 8. Results for the nematic director angle projection θ_{yz} at different z positions along the microchannel in the hydrodynamic focusing experiments. (a) Comparison of measured θ_{yz} for the simple flow experiments (no hydrodynamic focusing) at $Q = 3$ μL/min using the SSRL (green) and cSAXS (blue, finer beam size) beamlines. Even with the loss in spatial resolution due to the ca. 5-fold-larger X-ray beam at SSRL, which also shifts θ_{yz} to lower values, the same overall evolution in director rotation is observed. (b) Comparison between the simple flow and hydrodynamic focusing systems. The symbols represent measured θ_{yz}, and the lines are guides for the eye. The z position is rescaled by centering the director angle $\theta = 0°$ at $z_{rescaled} = 0$ μm.

the nematic stream, which enlarges the range in z over which the nematic phase gives a signal. More importantly, the averaging effects due to beam size also modify the observed values of θ_{yz}. In Figure 8a, a comparison of the simple flow system (i.e., no hydrodynamic focusing) with the small (fwhm ≈ 6 μm, blue circles) and large (fwhm ≈ 30 μm, green squares) beams can be seen. The curves are slightly different, with the data from the larger beam showing a shift to smaller θ_{yz} angles. Despite this, the same overall trend is still observed, which allows the characterization of the system. The shift in θ_{yz} to smaller angles is easily understood if one recalls that θ_{yz} has opposite signs in the upper and lower halves of the microchannel. If the beam is large enough that it partially overlaps both halves, then the opposite signs of θ_{yz} partially cancel each other, making the observed angle θ_{yz} smaller. This effect is more significant for narrower 5CB streams because the θ_{yz} variations are more compressed in space, accentuating the smearing from the larger beam size. In Figure 8b, $|\theta_{yz}|$ versus z curves are shown for different r_Q. Even with the finite beam size effects, clear differences in the slopes of the different curves are easily observed. It can be clearly seen that as r_Q increases from $r_Q = 0$ (simple flow experiments, green squares) to $r_Q = 8$ (blue circles) and to $r_Q = 24$ (red diamonds), the variation of $|\theta_{yz}|$ with z also increases.

Compared to the simple flow experiments, fitting the hydrodynamic focusing data is now significantly more complex. Now, parameters such as the viscosity mismatch, nematic sheet width, and interfacial curvature, among others, should clearly play a role in the velocity profile across the nematic sheet, which in turn should reflect on the measured θ_{yz} profile. In addition, the nonideal resolution along z (combination of large beam size and large step size) smears the measured θ_{yz} profiles significantly. As such, rather than fitting the data, we perform a qualitative analysis. Lockwood et al.[46] have shown that surfactants with branched chains (as is the case for Triton X-

100) have a tendency to induce planar alignment in nematics. Here we clearly observe a tilt in the director, which is also seen to increase as r_Q is increased. We note that the observed shift in θ_{yz} to larger angles as r_Q is increased (Figure 8b) should be even larger in reality because of the above-mentioned averaging effects due to the large beam size (that reduce the measured θ_{yz} to lower values). Hence, as the nematic stream gets narrower, we can conclude that the average angle θ_{yz} increases substantially. What is not clear is whether this angle is approximately constant or varies smoothly across the stream width. In either case, these observations seem more consistent with a picture where Triton X-100 imposes an angle/tilt at the interface (i.e., homeotropic anchoring or some angle intermediate between 90 and 0°) rather than planar alignment. We note that if Triton was imposing planar alignment under these (flow) conditions, then it should be imposing the same orientation as flow. Then, at most (as the ELP theory predicts), a shear angle of $\pm\theta_S$ could be observed across the nematic sheet as a result of flow, but this angle should not increase when the nematic stream becomes narrower at higher r_Q, as we observe in the results.

This work is the first step toward more detailed explorations and characterizations of the formation of nematic sheets and flowing liquid interface effects. In future work, an improved spatial resolution (achieved with smaller beam sizes) will be employed, along with a systematic variation of other surfactants with different anchoring properties (e.g., nonbranched alkyl chain surfactants that are known to impose homeotropic alignment and bolaamphiphile surfactants, that are known to impose planar alignment[47]), to look for their effects on the nematic sheets. We anticipate that the coupling of flow with the different anchoring properties of different materials (e.g., surfactants, lipids, polymers, and proteins)[48] will give rise to a wealth of interesting phenomena for both fundamental and applied fields. We also stress that this method can be applied to many different materials in a high-throughput fashion, which can be particularly useful for LC displays, where switching orientations are known to induce local flows, and for boundary lubrication, where the orientations of LCs under flow determine the tribological response of this type of material.

4. CONCLUSIONS

In this work, we investigated the interplay between flow and boundary condition effects on the orientation field of a thermotropic nematic liquid crystal under flow and confinement by using a combination of microfluidics with in situ SAXS. Two different experiments were performed. In the first, a nematic liquid crystal flowed through a square-channel cross section at varying flow rates, and the projection of the nematic director angle on the y−z shear plane was measured. At moderate-to-high flow rates, the director was found to be predominantly aligned in the flow direction, but with a small tilt angle of $\sim\pm11°$ in the velocity gradient direction, in agreement with the Leslie solution for Poiseuille flow. At low flow rates, a flow profile with a resemblance to the escaped radial director was observed, with the director varying more smoothly from the edges to the center of the channel.

In the second experiment, hydrodynamic focusing was employed to confine the nematic phase in a thin sheet sandwiched between two Triton X-100 aqueous solutions. The average director orientation was found to tilt by some amount away from the flow direction toward the liquid boundaries, although it remains unclear if one tilt angle is dominant through

most of the nematic sheet or if the tilt angle varies smoothly between two extreme values (~90 and 0°). We anticipate that expanding these studies to materials with different anchoring properties will give rise to a wealth of new phenomena under flow, which is interesting for both fundamental and applied sciences. In particular, this method can be used for high-throughput routine measurements to assess the influence of different surfactants or other additives on the orientation of nematic phases, which can lead to further improvements in areas such as boundary lubrication and LCDs.

ASSOCIATED CONTENT

Ⓢ Supporting Information

Additional details on the flow conditions for the simple flow and hydrodynamic focusing experiments. Discussion of the origin of the asymmetry in the $\theta_{YZ}(z)$ profile. A more detailed description of the fitting procedure for the $\theta_{YZ}(z)$ profile. This material is available free of charge via the Internet at http://pubs.acs.org.

AUTHOR INFORMATION

Corresponding Authors
*E-mail: brunobrasdasilva@gmail.com.
*E-mail: safinya@mrl.ucsb.edu.

Present Address
(N.V.) Departments of Mechanical Engineering and Biomolecular Science and Engineering, University of California, Santa Barbara, California 93106, United States.

Notes
The authors declare no competing financial interest.

ACKNOWLEDGMENTS

REFERENCES

(1) Stone, H. A.; Stroock, A. D.; Ajdari, A. Engineering Flows in Small Devices: Microfluidics Toward a Lab-on-a-Chip. *Annu. Rev. Fluid Mech.* **2004**, *36*, 381−411.

(2) Squires, T. M.; Quake, S. R. Microfluidics: Fluid Physics at the Nanoliter Scale. *Rev. Mod. Phys.* **2005**, *77*, 977−1026.

(3) Martinez, A. W.; Phillips, S. T.; Whitesides, G. M.; Carrilho, E. Diagnostics for the Developing World: Microfluidic Paper-Based Analytical Devices. *Anal. Chem.* **2010**, *82*, 3−10.

(4) Vlahovska, P. M.; Podgorski, T.; Misbah, C. Vesicles and Red Blood Cells in Flow: From Individual Dynamics to Rheology. *C. R. Phys.* **2009**, *10*, 775−789.

(5) Evans, H. M.; Dootz, R.; Köster, S.; Struth, B.; Pfohl, T. X-ray Microdiffraction on Flow-Controlled Biomolecular Assemblies. *Bull. Pol. Acad. Sci.: Tech. Sci.* **2007**, *55*, 217−227.

(6) Deschamps, J.; Kantsler, V.; Segre, E.; Steinberg, V. Dynamics of a Vesicle in General Flow. *Proc. Natl. Acad. Sci. U.S.A.* **2009**, *106*, 11444−11447.

(7) Pollack, L.; Tate, M. W.; Darnton, N. C.; Knight, J. B.; Gruner, S. M.; Eaton, W. A.; Austin, R. H. Compactness of the Denatured State of a Fast-Folding Protein Measured by Submillisecond Small-Angle X-ray Scattering. *Proc. Natl. Acad. Sci. U.S.A.* **1999**, *96*, 10115−10117.

(8) Otten, A.; Köster, S.; Struth, B.; Snigirev, A.; Pfohl, T. Microfluidics of Soft Matter Investigated by Small-Angle X-ray Scattering. *J. Synchrotron Rad.* **2005**, *12*, 745−750.

(9) Barrett, R.; Faucon, M.; Lopez, J.; Cristobal, G.; Destremaut, F.; Dodge, A.; Guillot, P.; Laval, P.; Masselon, C.; Salmon, J.-B. X-ray Microfocussing Combined with Microfluidics for on-Chip X-ray Scattering Measurements. *Lab Chip* **2006**, *6*, 494−499.

(10) Pfohl, T.; Otten, A.; Köster, S.; Dootz, R.; Struth, B.; Evans, H. M. Highly Packed and Oriented DNA Mesophases Identified Using in Situ Microfluidic X-ray Microdiffraction. *Biomacromolecules* **2007**, *8*, 2167−2172.

(11) Lafleur, J. P.; Snakenborg, D.; Nielsen, S. S.; Møller, M.; Toft, K. N.; Menzel, A.; Jacobsen, J. K.; Vestergaard, B.; Arleth, L.; Kutter, J. P. Automated Microfluidic Sample-Preparation Platform for High-Throughput Structural Investigation of Proteins by Small-Angle X-ray Scattering. *J. Appl. Crystallogr.* **2011**, *44*, 1090−1099.

(12) Santoro, G.; Buffet, A.; Döhrmann, R.; Yu, S.; Körstgens, V.; Müller-Buschbaum, P.; Gedde, U.; Hedenqvist, M.; Roth, S. V. Use of Intermediate Focus for Grazing Incidence Small and Wide Angle X-ray Scattering Experiments at the Beamline P03 of PETRA III, DESY. *Rev. Sci. Instrum.* **2014**, *85*, 043901.

(13) Cubaud, T.; Mason, T. Folding of Viscous Threads in Diverging Microchannels. *Phys. Rev. Lett.* **2006**, *96*, 114501.

(14) De Gennes, P.-G.; Prost, J. *The Physics of Liquid Crystals*, 2nd ed.; Oxford University Press: Oxford, U.K., 1993.

(15) Safinya, C. R.; Sirota, E. B.; Plano, R. J. Nematic to Smectic-A Phase Transition under Shear Flow: A Nonequilibrium Synchrotron X-ray Study. *Phys. Rev. Lett.* **1991**, *66*, 1986−1989.

(16) Safinya, C. R.; Sirota, E. B.; Bruinsma, R. F.; Jeppesen, C.; Plano, R. J.; Wenzel, L. J. Structure of Membrane Surfactant and Liquid Crystalline Smectic Lamellar Phases under Flow. *Science* **1993**, *261*, 588−591.

(17) Diat, O.; Roux, D.; Nallet, F. Effect of Shear on a Lyotropic Lamellar Phase. *J. Phys. II* **1993**, *3*, 1427−1452.

(18) Fernández-Nieves, A.; Cristobal, G.; Garcés-Chávez, V.; Spalding, G. C.; Dholakia, K.; Weitz, D. A. Optically Anisotropic Colloids of Controllable Shape. *Adv. Mater.* **2005**, *17*, 680−684.

(19) Fernández-Nieves, A.; Link, D. R.; Márquez, M.; Weitz, D. A. Topological Changes in Bipolar Nematic Droplets under Flow. *Phys. Rev. Lett.* **2007**, *98*, 087801.

(20) Hamlington, B. D.; Steinhaus, B.; Feng, J. J.; Link, D.; Shelley, M. J.; Shen, A. Q. Liquid Crystal Droplet Production in a Microfluidic Device. *Liq. Cryst.* **2007**, *34*, 861−870.

(21) Martel, A.; Burghammer, M.; Davies, R. J.; Di Cola, E.; Vendrely, C.; Riekel, C. Silk Fiber Assembly Studied by Synchrotron Radiation SAXS/WAXS and Raman Spectroscopy. *J. Am. Chem. Soc.* **2008**, *130*, 17070−17074.

(22) Martin, H. P.; Brooks, N. J.; Seddon, J. M.; Terrill, N. J.; Luckham, P. F.; Kowalski, A. J.; Cabral, J. T. Complex Fluids under Microflow Probed by SAXS: Rapid Microfabrication and Analysis. *J. Phys.: Condens. Matter* **2010**, *247*, 012050.

(23) Cuennet, J. G.; Vasdekis, A. E.; De Sio, L.; Psaltis, D. Optofluidic Modulator Based on Peristaltic Nematogen Microflows. *Nat. Photonics* **2011**, *5*, 234−238.

(24) Sengupta, A.; Tkalec, U.; Ravnik, M.; Yeomans, J. M.; Bahr, C.; Herminghaus, S. Liquid Crystal Microfluidics for Tunable Flow Shaping. *Phys. Rev. Lett.* **2013**, *110*, 048303.

(25) Trebbin, M.; Steinhauser, D.; Perlich, J.; Buffet, A.; Roth, S. V.; Zimmermann, W.; Thiele, J.; Förster, S. Anisotropic Particles Align Perpendicular to the Flow Direction in Narrow Microchannels. *Proc. Natl. Acad. Sci. U.S.A.* **2013**, *110*, 6706−6711.

(26) Håkansson, K. M. O.; Fall, A. B.; Lundell, F.; Yu, S.; Krywka, C.; Roth, S. V.; Santoro, G.; Kvick, M.; Wittberg, L. P.; Wågberg, L.; Soderberg, L. D. Hydrodynamic Alignment and Assembly of Nanofibrils Resulting in Strong Cellulose Filaments. *Nat. Commun.* **2014**, *5*, 4018.

(27) Lee, J.-H.; Kamal, T.; Roth, S. V.; Zhang, P.; Park, S.-Y. Structures and Alignment of Anisotropic Liquid Crystal Particles in a Liquid Crystal Cell. *RSC Adv.* **2014**, *4*, 40617−40625.

(28) Leslie, B. F. M. Some Constitutive Equations for Anisotropic Fluids. *Q. J. Mech. Appl. Math.* **1966**, *19*, 357−370.

(29) Ericksen, J. L. Anisotropic Fluids. *Arch. Ration. Mech. Anal.* **1960**, *4*, 231−237.

(30) Parodi, O. Stress Tensor for a Nematic Liquid Crystal. *J. Phys. (Paris)* **1970**, *31*, 581−584.

(31) Ozaki, R.; Aoki, M.; Yoshino, K.; Toda, K.; Moritake, H. Effective Viscosity for Nematic-Liquid-Crystal Viscosity Measurement Using a Shear Horizontal Wave. *Phys. Rev. E* **2010**, *81*, 061703.

(32) Hamley, I.; Castelletto, V.; Parras, P. Small-Angle X-ray Scattering Study of Flow Alignment of a Thermotropic Liquid Crystal in the Nematic and Smectic Phases. *Phys. Rev. E* **2006**, *74*, 020701.

(33) Castelletto, V.; Squires, A. M.; Hamley, I. W.; Stasiak, J.; Moggridge, G. D. A SAXS Study of Flow Alignment of Thermotropic Liquid Crystal Mixtures. *Liq. Cryst.* **2009**, *36*, 435−442.

(34) Knight, J.; Vishwanath, A.; Brody, J.; Austin, R. Hydrodynamic Focusing on a Silicon Chip: Mixing Nanoliters in Microseconds. *Phys. Rev. Lett.* **1998**, *80*, 3863−3866.

(35) Anna, S. L.; Bontoux, N.; Stone, H. A. Formation of Dispersions Using "Flow Focusing" in Microchannels. *Appl. Phys. Lett.* **2003**, *82*, 364−366.

(36) Fletcher, B.; Rosales, M. Z.; Silva, B. F. B. Flexible and customized male Luer adapters with low dead-volume requirements http://blogs.rsc.org/chipsandtips/2013/04/16/flexible-and-customized-male-luer-adapters-with-low-dead-volume-requirements/.

(37) Qiao, L.; Easteal, A. J. Mass Transport in Triton X Series Nonionic Surfactant Solutions: A New Approach to Solute-Solvent Interactions. *Colloid Polym. Sci.* **1996**, *274*, 974−980.

(38) Cladis, P. E.; Bogardus, R. K.; Aadsen, D. High-Pressure Investigation of the Reentrant Nematic Bilayer Smectic-A Transition. *Phys. Rev. A* **1978**, *18*, 2292−2306.

(39) Davidov, D.; Safinya, C. R.; Kaplan, M.; Dana, S. S.; Schaetzing, R.; Birgeneau, R. J.; Litster, J. D. High-Resolution X-ray and Light-Scattering Study of Critical Behavior Associated with the Nematic-Smectic-A Transition in 4-Cyano-4′-Octylbiphenyl. *Phys. Rev. B* **1979**, *19*, 1657−1663.

(40) Jewell, S. A.; Cornford, S. L.; Yang, F.; Cann, P. S.; Sambles, J. R. Flow-Driven Transition and Associated Velocity Profiles in a Nematic Liquid-Crystal Cell. *Phys. Rev. E* **2009**, *80*, 041706.

(41) Cladis, P. E.; Kléman, M. Non-Singular Disclinations of Strength S = + 1 in Nematics. *J. Phys. (Paris)* **1972**, *33*, 591−598.

(42) Allender, D. W.; Crawford, G. P.; Doane, J. W. Determination of the Liquid-Crystal Surface Elastic Constant K24. *Phys. Rev. Lett.* **1991**, *67*, 1442−1445.

(43) Helgeson, M. E.; Porcar, L.; Lopez-Barron, C.; Wagner, N. J. Direct Observation of Flow-Concentration Coupling in a Shear-Banding Fluid. *Phys. Rev. Lett.* **2010**, *105*, 084501.

(44) Cubaud, T.; Mason, T. G. Capillary Threads and Viscous Droplets in Square Microchannels. *Phys. Fluids* **2008**, *20*, 053302.

(45) Delabre, U.; Richard, C.; Cazabat, A. M. Some Specificities of Wetting by Cyanobiphenyl Liquid Crystals. *J. Phys.: Condens. Matter* **2009**, *21*, 464129.

(46) Lockwood, N. A.; de Pablo, J. J.; Abbott, N. L. Influence of Surfactant Tail Branching and Organization on the Orientation of Liquid Crystals at Aqueous - Liquid Crystal Interfaces. *Langmuir* **2005**, *21*, 6805−6814.

(47) Brake, J. M.; Mezera, A. D.; Abbott, N. L. Effect of Surfactant Structure on the Orientation of Liquid Crystals at Aqueous - Liquid Crystal Interfaces. *Langmuir* **2003**, *19*, 6436−6442.

(48) Lockwood, N. A.; Gupta, J. K.; Abbott, N. L. Self-Assembly of Amphiphiles, Polymers and Proteins at Interfaces between Thermotropic Liquid Crystals and Aqueous Phases. *Surf. Sci. Rep.* **2008**, *63*, 255−293.